Advanced Functional Materials

ADVANCED FUNCTIONAL MATERIALS
www.afm-journal.de

RESEARCH ARTICLE OPEN ACCESS

Si-Doped Nanocrystalline Diamond as Highly Sensitive Luminescence Thermometer for the Physiological Temperature Range

María Gragera[1] | Iván Carrillo-Berdugo[1] | Josue Millán[2] | Paulius Pobedinskas[3,4] | Antonio Freire[2] | Ken Haenen[3,4] | Javier Navas[1]

[1]Department of Physical Chemistry, University of Cadiz, Cádiz, Spain | [2]Department of Science Materials and Metallurgic Engineering and Inorganic Chemistry, IMEYMAT, University of Cadiz, Cádiz, Spain | [3]Institute for Materials Research (IUMAT), Hasselt University, Hasselt, Belgium | [4]IUMAT, imec, Diepenbeek, Belgium

Correspondence: Iván Carrillo-Berdugo (ivan.carrillo@uca.es) | Javier Navas (javier.navas@uca.es)

Received: 18 February 2026 | **Revised:** 24 June 2026 | **Accepted:** 13 July 2026

Keywords: diamond | luminescent thermometry | SiV^- centers

ABSTRACT

Si-doped nanodiamonds are emerging as highly promising materials for luminescent thermometry in the physiological temperature range (300–325 K) due to their excellent biocompatibility, chemical inertness, and optical transparency, as well as their ability to host negative charged silicon-vacancy (SiV^-) centers with sharp, photostable emission within the biological transparency windows. In this work, Si-doped nanocrystalline diamond thin films were synthesized on silicon substrates via microwave plasma-enhanced chemical vapor deposition (MPECVD) under various growth pressures and methane flow conditions, aiming to obtain the practical boundary limit of the photoluminescence intensity. The temperature dependence of key photoluminescence parameters, including intensity, full width at half maximum (FWHM), and area of the zero-phonon line emission, was investigated in the physiological range (300–325 K). The experimental photoluminescence results were interpreted with the support of first-principles density functional theory calculations, linking the defect electronic structure and electron–phonon coupling to the observed optical response. By employing multiparametric analysis, combining these thermally sensitive luminescence features in a single model, a self-calibrated approach for robust thermometry was demonstrated, optimizing the thermal sensitivity of the SiV^- centers-based emission of the MPECVD diamond. A maximum relative thermal sensitivity of 2.3% K^{-1} was achieved, highlighting the potential of Si-doped nanodiamonds for accurate and minimally invasive temperature monitoring in complex biological environments.

1 | Introduction

Precise temperature monitoring at the nanoscale is essential for unveiling the role of thermal fluctuations in cellular processes, regulating metabolic activity [1], and guiding advanced biomedical therapies such as hyperthermia, photothermal therapy, and controlled drug release [2, 3]. Among the different approaches developed for nanoscale thermometry, luminescent nanothermometry has emerged as a powerful technique due to its non-invasive nature, high spatial resolution, and ability to operate in complex biological environments [4].

To be effective in vivo, nanothermometers must combine high thermal sensitivity with biocompatibility, chemical stability, and long-term photostability, while operating within the optical transparency windows of biological tissue [5]. These

requirements have motivated the exploration of a wide range of luminescent nanothermometers, including organic dyes, polymeric nanogels, semiconductor quantum dots, perovskite nanocrystals, and lanthanide-based nanoparticles. However, despite significant progress, each of these platforms presents critical limitations that restrict their clinical translation. Organic dyes and nanogels, for instance, exhibit high thermal sensitivity but are susceptible to photobleaching, local environmental fluctuations, and typically emit outside the biological transparency windows, reducing light penetration in tissue [6, 7]. Quantum dots and perovskite nanocrystals can be tuned into the near-infrared range [8], but their chemical and photonic instability in the physiological temperature range remains a major challenge. Lanthanide-based up-conversion nanoparticles, while offering environment-independent emission, suffer from intrinsically weak absorption and low quantum yields, which ultimately limit brightness and temperature resolution [9, 10].

Si-doped nanodiamonds provide a promising solution to these challenges. Luminescence thermometry based on SiV^- (negative charged silicon-vacancy) centers in diamond exploits the temperature dependence of their optical emission properties. Temperature variations induce changes in the electronic structure and electron–phonon interactions of the SiV^- centers, resulting in measurable shifts of the zero-phonon line, spectral broadening, and modifications of the luminescence intensity. By optically monitoring these temperature-dependent spectral features, the local temperature can be determined in a non-contact and highly sensitive manner. This approach combines the exceptional photostability of diamond color centers with high spatial resolution and accuracy for temperature sensing. Also, diamond is a chemically inert, highly biocompatible, and optically transparent host material, with negligible cytotoxicity and exceptional stability under the physiological temperature range. Embedded within this robust lattice, SiV^- centers exhibit sharp, stable, and photostable emission dominated by a zero phonon line (ZPL) at about 738 nm, located within the first biological transparency window. This enables deep-tissue optical access with reduced scattering, low autofluorescence, and minimal photodamage compared to visible emitters. Furthermore, the inversion symmetry of the SiV^- defect provides remarkable spectral stability against environmental perturbations, while its high Debye–Waller factor ensures a large fraction of the emission is concentrated in the ZPL [11, 12]. These properties make SiV^- centers as one of the most suitable optical probes for luminescent nanothermometry in complex biological environments.

Recently, the reliability of luminescent nanothermometers has been significantly enhanced through multiparametric approaches, where temperature simultaneously affects distinct luminescent properties, such as spectral position, linewidth, or intensity. By combining multiple thermometric parameters, these nanothermometers provide self-calibrated readouts that minimize the influence of fluctuations in probe concentration, excitation power, or detection conditions, ultimately improving both sensitivity and accuracy. In this context, multiple linear regression (MLR) emerges as a powerful analytical framework to fully exploit the information contained in multiparametric luminescence. MLR enables the integration of several temperature-dependent parameters into a single predictive model [13]. This statistical approach can markedly enhance performance, providing more precise and robust temperature measurements in the physiological temperature range in biomedical scenarios where experimental variability is inevitable [14].

While SiV-based thermometry has been extensively demonstrated in bulk single-crystal diamond (SCD) and top-down fabricated nanostructures [15–17]. the translation of this technology to the physiological temperature range remains hindered by the scalability, cost, and geometric limitations of SCD. This study addresses this critical materials challenge by using nanocrystalline diamond (NCD) thin films. NCD offers a highly scalable, conformal alternative that can be directly integrated into biosensing platforms, provided the thermal sensitivity of the SiV centers can be maintained amidst the higher grain boundary density. In addition, while our previous work demonstrated the feasibility of luminescence thermometry in N-/Si-co-doped NCD films utilizing dual NV/SiV emissions [18], the presence of nitrogen inherently alters the CVD growth kinetics, increasing grain boundary density and introducing broad NV phonon sidebands that can convolute spectral readout in biological tissues. The present study eliminates nitrogen to focus exclusively on pure Si-doped NCD. By isolating the SiV defect within a higher-purity sp^3 matrix, we achieve a high-contrast, background-free ZPL at ~738 nm, strategically optimizing the spectral purity and thermal sensitivity specifically for the narrow-window (300–325 K) physiological temperature range. Therefore, in this study, Si-doped nanocrystalline diamonds were grown on silicon substrates using microwave plasma-enhanced chemical vapor deposition (MWPECVD). The synthesis was carried out under a range of growth conditions to evaluate the influence of growth pressure and methane flow on the photoluminescence (PL) behavior of the nanodiamonds, as well as to identify the conditions that maximize emission intensity. The temperature dependence of key photoluminescence parameters, including intensity, FWHM, and the area of the ZPL of SiV^- centers, was studied within the physiological temperature range (300–325 K) to assess their potential for multiparametric photoluminescent thermometry. In addition, first-principles simulations of PL line-shapes for SiV^- and SiV^0 point defects were performed to gain insight into the electronic structure, the charge-dependency, and the electron–phonon coupling underlying optical transitions of these centers. If experiments prove such simulations can be predictive, these could become a key tool to screen candidate point defects and host materials for temperature sensing applications in biological contexts.

2 | Results and Discussion

2.1 | Diamond Characterization

2.1.1 | Varying Growth Pressure

As was described previously, diamond films were grown at different pressures (40, 45, 55, 65, and 80 Torr) to evaluate the influence of this parameter on both the crystallinity of the diamond and the incorporation of Si. The crystalline structure of the films was analyzed by x-ray diffraction (XRD). Figure 1a presents the diffractograms of all samples in the 40°–80° range to highlight the diamond peaks: two prominent peaks are observed

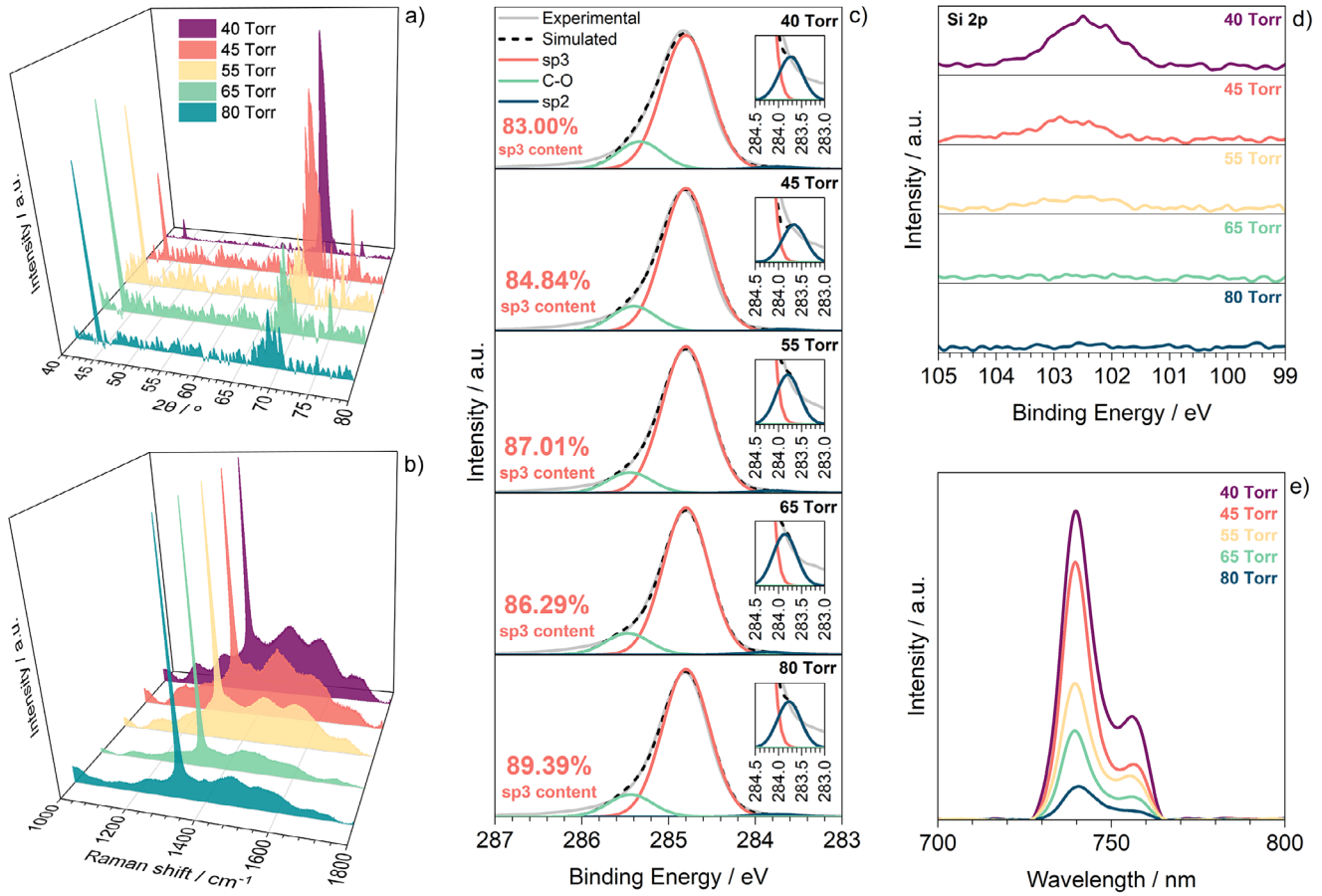

FIGURE 1 | (a) Diffractograms obtained from XRD; (b) Raman spectra; high-resolution XP spectra for (c) C 1s, and (d) Si 2p regions; and (e) steady-state PL spectra of the samples grown at different pressures.

in all cases at 2θ values about 43.8° and 75.2°, corresponding to the (111) and (220) diffraction planes of cubic diamond, respectively [19, 20]. No signals corresponding to amorphous carbon (typically at 26.3° and 68.9°) or graphite (29.3° and 47.3°) are detected in any sample [21], as is observed in Figure S1, which shows the complete XRD patterns. Additionally, the characteristic peak of the (004) plane of the silicon <100> substrate, located at 68.8°, is present in all diffractograms [22]. As the growth pressure increases, the intensity of the diamond (111) peak becomes progressively stronger, indicating an improvement in crystallinity.

To confirm the successful synthesis of diamond and to investigate the possible presence of other carbon allotropes in the samples, Raman spectroscopy was performed. Figure 1b displays the Raman spectra of the Si-doped diamond films. All spectra exhibit the characteristic sharp peak of crystalline diamond at approximately 1333 cm^{-1}, which corresponds to the first-order optical phonon mode of T_{2g} symmetry [23]. Raman spectroscopy also enables the identification of other carbon phases, particularly graphite. For simplicity in describing its vibrational properties, graphite is often considered a multilayer form of graphene, given the weak interlayer interactions. Among the six phonon modes of graphene at the Brillouin zone center, only the E_{2g} optical phonon mode is Raman active. The so-called G band originates from this E_{2g} mode and is typically located at 1583 cm^{-1}. This mode involves in-plane vibrations of the carbon atoms [24]. This band is present in all our spectra and becomes more pronounced as the deposition pressure decreases. In addition, a weak shoulder close to the diamond peak at ~1370 cm^{-1} is only barely discernible in our spectra. This signal corresponds to the disorder-induced D band [25], thus, the low intensity observed indicates a low concentration of structural disorder in the samples. Additionally, a broadband centered around 1490 cm^{-1} is observed in all samples, which is associated with the $\nu 3$ trans-polyacetylene (TPA) mode located at grain boundaries. The $\nu 1$ TPA band, typically appearing between 1100 and 1200 cm^{-1}, is detected only in the samples grown at lower deposition pressures [26]. Overall, the non-diamond bands (G, D, and TPA) are significantly more pronounced at lower deposition pressures, while the characteristic diamond band is more intense at higher pressures, which is consistent with XRD results. These observations suggest that deposition pressure plays a significant role in the incorporation of sp^2-carbon phases and in the development of boundary-related vibrational features in the films, as discussed from XPS results next. Thus, while the bulk volume is highly crystalline, as discussed from XRD, Raman spectroscopy reveals the expected presence of non-diamond (sp^2) carbon phases. Due to the nanocrystalline morphology of the films, the high density of grain boundaries intrinsically introduces sp^2-bonded carbon. Because visible Raman spectroscopy is highly sensitive to sp^2 carbon, more than 50 times higher than for sp^3 diamond [27], these non-diamond features are prominently visible in the spectra, accurately reflecting the complex composite

nature (sp^3 grains surrounded by sp^2 boundaries) characteristic of NCD films. In addition, measurements by FTIR spectroscopy were performed to confirm the diamond growth. Figure S2 shows the spectra obtained, where typical C–H stretch peaks for diamond grown by CVD at about 2850 and 2920 cm^{-1} are clearly observed [15].

To gain further insight into the chemical composition and chemical state bonding of the Si-doped diamond films, x-ray photoelectron spectroscopy (XPS) measurements were performed. Survey spectra registered are shown in Figure S3. The expected presence of C and O is confirmed in all the grown diamonds. High-resolution C 1s core-level spectra were analyzed to quantify the sp^3 content of the films. Figure 1c shows the high-resolution C 1s spectra of the diamond films. The C 1s spectra of all samples were deconvoluted into distinct components corresponding to sp^2 and sp^3 carbons and C—O bonds, typically observed at binding energies of ~284.4, 285.2, and 286.3 eV, respectively [28]. As the deposition pressure increases, a progressive increase in the sp^3 fraction is observed, indicating a higher proportion of tetrahedrally bonded carbon in the films. This trend is consistent with Raman results, where higher pressures yielded weaker sp^2-related bands. Although variations in the sp^3 content are evident across the samples, all films exhibit a relatively high sp^3 fraction, ranging between 80% and 90%.

The systematic increase in non-diamond components (such as sp^2 and amorphous carbon) observed in the XRD, Raman, and XPS analyses as the deposition pressure decreases can be attributed to the fundamental plasma dynamics of the CVD process. In diamond CVD, reactive atomic hydrogen is critical for maintaining phase purity, as it preferentially etches graphitic (sp^2) carbon at a much higher rate than the diamond (sp^3) phase [29]. As the deposition pressure is reduced, the plasma density decreases, leading to a lower thermal dissociation rate of H_2 and, consequently, a reduced flux of H* to the growth [30]. This diminished supply of atomic hydrogen severely reduces the etching efficiency of non-diamond carbon. Furthermore, the increased mean free path of gas species at lower pressures can alter the kinetic energy of impinging radicals, promoting secondary nucleation and the formation of sp^2-rich grain boundaries [31]. Consequently, the suppression of the H* etching mechanism at lower pressures leads to the gradual accumulation of the non-diamond phases observed in our spectroscopic data, which in turn influences the host matrix quality for SiV center formation.

On the other hand, high-resolution Si 2p spectra reveal the presence of silicon in some samples Figure 1d, mainly in those grown at lower deposition pressures. Notably, the Si 2p peak appears at around 102 eV, consistent with Si—O—C bonding [32], rather than the elemental Si from the <100> substrate, which would be expected around 99 eV [33]. This indicates that the observed Si signal corresponds to silicon incorporated into the diamond lattice or in associated chemical environments. Interestingly, in the films grown at the highest pressures (65 and 80 Torr), the Si signal is no longer detectable. Overall, the XPS analysis confirms the successful growth of diamond films with a predominantly sp^3 bonding character and provides further evidence that higher deposition pressures promote improved crystallinity, while lower pressures lead to higher Si content in the diamonds.

The emission features of the Si-doped diamond films were further investigated through photoluminescence spectroscopy. All spectra were recorded at room temperature using a 633 nm excitation laser with an acquisition time of 7 s, 7 accumulations, and a 10% ND filter. To accurately analyze the emission associated with the negatively charged silicon-vacancy centers (SiV^-), all spectra were post-processed by removing the baseline, thereby isolating the signal corresponding to the SiV^- center and its phonon sideband (PSB). Figure 1e shows the PL spectra of the samples. The ZPL of the SiV^- center is observed at 739.4 nm, while the associated phonon side band (PSB) appears at 755.6 nm [34]. A clear trend is evident: as the deposition pressure increases, the emission intensity of the SiV^- centers decreases. This behavior can be directly related to the chemical and structural characteristics of the films discussed earlier. XPS analysis showed that the silicon content in the films is reduced at higher pressures, with the Si signal becoming negligible in the samples grown at 65 and 80 Torr. Similarly, XRD results indicate that higher-pressure growth produces NCD films with less structural defects. These observations suggest that crystal quality is worse when more Si is incorporated, while highly ordered diamond networks are obtained with less Si.

Consequently, the decrease in SiV^- emission with increasing pressure is consistent with the reduced incorporation of silicon into the diamond lattice. In addition, the increase in sp^3 content and overall crystallinity at higher pressures, as revealed by XPS and Raman spectroscopy, indicates that high-quality NCD films were obtained and less accommodating for the formation of SiV^- centers. In other words, higher-pressure growth promotes high-quality diamond films with fewer Si-related centers, resulting in lower PL intensity from SiV^- centers despite the improved structural properties.

Therefore, based on the PL results, the lowest deposition pressure of 40 Torr was selected, as it exhibits the highest SiV^- emission intensity. Although structural characterization indicates that films grown at higher pressures display slightly improved crystallinity and higher sp^3 content, the sample grown at 40 Torr still presents excellent diamond quality, with a high sp^3 fraction (83%) and minimal non-diamond carbon phases. In addition, the PL emission was also measured by using a 473 nm excitation laser (see Figure S4). Again, the highest emission intensity was observed for the sample grown at 40 Torr. Other emission features were observed between 550 and 700 nm, which is typical in diamond grown by CVD.

It is important to note that the highest SiV^- ZPL intensity was observed at 40 Torr Figure 1e, the lowest pressure investigated in this series. The 40 Torr represents a practical lower boundary for functional NCD growth in our specific clam-shell reactor configuration. This boundary was established to balance the competing kinetic requirements of the system: exploiting the lower pressure to enhance Si-radical transport, while preventing the severe drop-in growth rate associated with low-pressure regimes. Furthermore, compensating for this rate drop by increasing the CH_4 concentration was deliberately avoided to preserve the high sp^3/sp^2 phase purity required for optical sensing. Thus, the 40 Torr and 1% CH_4 regime serves as a functional optimum that maximizes Si incorporation without compromising the structural integrity of the diamond matrix. Thus, 40 Torr was the pressure

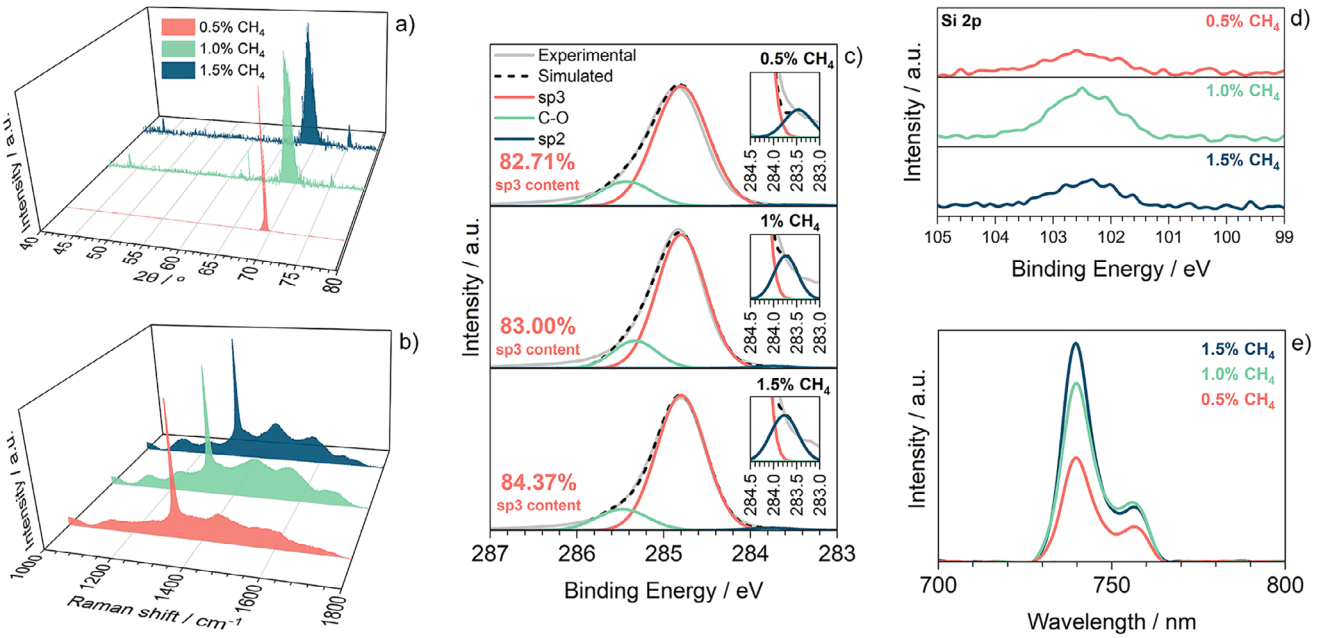

FIGURE 2 | (a) Diffractograms obtained from XRD; (b) Raman spectra; high-resolution XPS spectra for (c) C 1s, and (d) Si 2p regions; and (e) steady-state PL spectra of the samples grown at 40 Torr and different methane concentrations.

chosen for further investigations focused on the influence of methane concentration. For this, a set of samples was grown with the pressure fixed at 40 Torr while varying the CH_4 content (0.5%, 1.0%, and 1.5%). These samples were characterized using the same XRD, Raman, XPS, and PL techniques to systematically evaluate the effect of methane concentration on both structural and optical properties.

2.1.2 | Varying Methane Concentration

XRD patterns confirm the formation of crystalline diamond under all conditions (Figure 2a). However, clear differences are observed in the relative intensities of the diffraction peaks. At 0.5% CH_4, the diamond (111) peak at 43.8° is present but shows very low intensity, and the (220) reflection at 75.2° is not detected, indicating limited crystalline quality and/or weak preferential orientation. In contrast, at 1.0% and 1.5% CH_4, both the (111) and (220) reflections are clearly observed, revealing a better-developed crystalline structure and a higher degree of orientation in the films grown under more carbon-rich CVD conditions.

Raman spectroscopy reveals the characteristic sharp peak of diamond at 1333 cm^{-1} in all samples. As the methane fraction increases, disorder-related bands become more prominent, particularly the G band at 1583 cm^{-1} and the broad TPA feature around 1490 cm^{-1}, as shown in Figure 2b. This indicates that excess methane promotes a higher degree of disorder compared to samples grown with lower CH_4 concentrations, which leads to the incorporation of sp^2 phases at grain boundaries.

Interestingly, XPS provides complementary information that helps reconcile these observations. As shown in Figure 2c, the relative sp^3 fraction increases with methane concentration, reaching its maximum at 1.5% CH_4. This trend appears opposite to Raman, but it can be rationalized by considering the different probing depths and sensitivities of the techniques. The surface, with large, well-facetted grains and less grain boundaries, is of higher quality than deeper in the film. Thus, although additional methane increases surface disorder detected by Raman, corresponding more to the subsurface, while leading to a higher average sp^3 content in XPS, which is related to the surface. But we have to note the variations of the sp^3 content are slight. In addition, high-resolution Si 2p spectra (Figure 2d) further support this interpretation. A Si 2p component centered around ~102 eV is detected in all samples, consistent with oxidized or Si—O—C environments rather than substrate silicon. Importantly, the Si 2p intensity is lowest at 0.5% CH_4 and increases for 1.0% and 1.5% CH_4, indicating a higher incorporation of silicon-related species within the films as the methane concentration rises.

Finally, PL was employed to evaluate the optical properties of the films Figure 2e. All spectra were acquired and processed under the same conditions as the previous measurements, with baseline correction applied to isolate the signal of the SiV^-. The characteristic ZPL of the SiV^- centers is observed at 739.4 nm, along with its PSB at approximately 755 nm. A clear dependence on methane concentration is found: the lowest CH_4 content (0.5%) yields the weakest emission, while the PL intensity progressively increases with higher methane concentration, reaching a maximum at 1.5%. This behavior is consistent with the XPS results, indicating that carbon-rich growth conditions promote the incorporation of silicon into the diamond lattice, favoring the formation of optically active SiV^- centers. Again, FTIR, the XPS survey spectra and luminescence emission by using a 473 nm excitation laser are included in the (Figures S2–S4) as complementary evidence of this discussion.

Overall, these results show that increasing methane concentration enhances diamond crystallinity, which is unexpected, but in

TABLE 1 | Growth conditions of samples.

p [Torr][a]	CH_4 [%]	t [b]	T [°C] [c]	h [nm] [d]	*size* [mm × mm]
40	1.0	3 h 37 min	740	1215	5.03 × 5.04
45	1.0	2 h 43 min	775	1080	5.05 × 5.06
55	1.0	2 h 56 min	790	1125	5.04 × 5.06
65	1.0	3 h 15 min	820	1170	5.04 × 5.06
80	1.0	3 h 17 min	880	1080	5.04 × 5.05
40	0.5	5 h 15 min	735	1080	5.03 × 5.06
40	1.5	2 h 59 min	750	1395	5.04 × 5.06

[a] p: pressure.
[b] t: time.
[c] T: temperature.
[d] h: thickness.

this case, this increase in crystallinity can be explained by the greater thickness of the diamond grown with a higher methane concentration (Table 1). Also, increasing methane concentration enhances the orientation on the microscale (as revealed by XRD), while simultaneously increasing surface disorder and grain-boundary sp^2 phases (as detected by Raman). At the same time, XPS demonstrates an overall increase in sp^3 bonding and higher Si incorporation within the near-surface region, which is reflected in the stronger SiV^- photoluminescence. Considering all structural and optical indicators, the film grown at 1.0% CH_4 represents an optimal compromise: it exhibits well-defined diamond diffraction peaks, moderate surface disorder, a high sp^3 fraction, and intense SiV^- emission. Therefore, the sample synthesized at 40 Torr and 1.0% CH_4 was selected for further analysis.

2.1.3 | Electronic Structure and Simulated PL Line-Shapes

Motivated by the experimental results, we employed first-principles density functional theory (DFT) simulations to understand the robust SiV^- emission observed in our diamond samples in terms of the electronic structure, the charge-dependency and the electron-phonon coupling underlying optical transitions of this center, thereby providing a microscopic interpretation of the observed luminescence.

The introduction of the SiV center into the diamond lattice generates well-defined electronic states within the band gap for both SiV^- and SiV^0 charge states, as illustrated in Figure 3a,b. Notably, the defect bands exhibit minimal dispersion along the high-symmetry k-path, indicating that the associated electronic states are strongly localized around the SiV center. This strong localization naturally explains the narrow ZPLs observed experimentally for SiV centers. The corresponding DOS and PDOS diagrams, provided in Figure S5, confirm that the wide diamond band gap is preserved and demonstrate that these localized in-gap levels originate from the hybridization of s- and p-type orbitals of the Si atom and its nearest-neighbor C atoms in the split-vacancy configuration, based on the partial contributions of these orbitals to the total DOS.

The featured excited-state configurations for the SiV^- and SiV^0 centers are a doublet and a triplet state, respectively. The calculated ZPL energies are 1.70 eV (729 nm) for SiV^- and 1.52 eV (816 nm) for SiV^0. The energy value for the SiV^- center is in excellent agreement with respect to the experimental result (1.68 eV for SiV^-) and previous ab initio studies [36], although the one for the SiV^0 center differs by *ca* 0.2 eV (1.31 eV reported in experimental literature) [37]. This is beyond the intrinsic limitations of the exchange-correlation approximations in DFT, finite-size effects or charge corrections inherent to defect calculations in periodic frameworks [38]. The SiV^0 center has an unusually complex electronic structure in which orbital reordering occurs (the emptied e_g states shift above the valence band) and the degeneracy between e_u states and e_g states requires precise constraints on the desired orbitals [39]. We have considered all that in our CDFT simulations and found a 1.52 eV ZPL, in agreement with previously reported values at this level of theory [40, 41].

To probe the optical transitions associated with the SiV^- and SiV^0 centers, we used the PyPhotonics workflow, based on the generating function approach. The simulated PL line shapes are shown in Figure 3c. The Huang-Rhys factor values, 0.167 and 0.170 for SiV^- and SiV^0 centers, respectively, inform of a relatively weak electron-phonon coupling for both, resulting in a prominent ZPL accompanied by a weak PSB in both charge states.

The simulations reproduce the spectral line shape and the relative intensities remarkably well, in agreement with our experimental observations for SiV^- centers, where under 633 nm laser excitation only SiV^- emission is detected, and any contribution from SiV^0 remains effectively undetectable due to the low excitation efficiency of its optical transition at this wavelength. Overall, the consistency between simulations and experiments validates the present computational framework for the purpose of screening point defects and host materials based on relative comparisons. If absolute predictions are required, more sophisticated methods like hybrid functionals or the GW approximation should be used, computational resources permitting. Other authors have made efforts in that way to accurately describe the electronic structures and PL spectral features of NV^- centers in diamond [42–44]. We aimed for a streamlined, robust approach for preliminary material

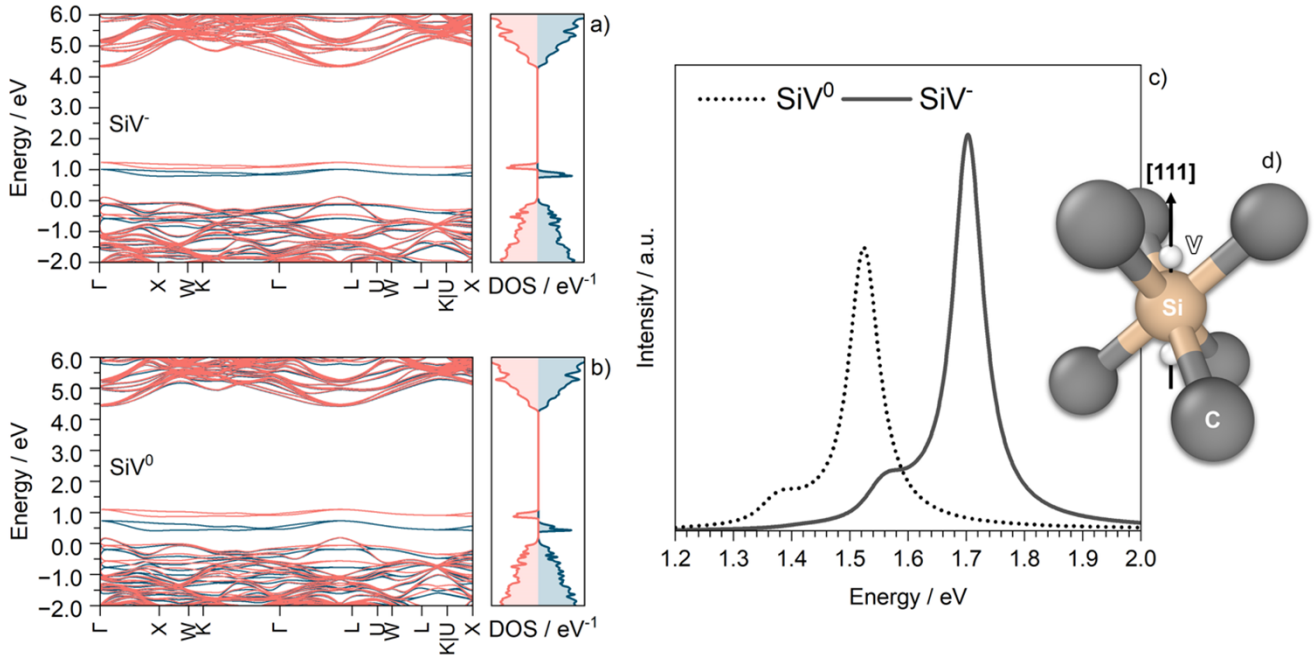

FIGURE 3 | Band structures and density of states of (a) SiV^- and (b) SiV° centers, where blue corresponds to the spin-down channel and red to the spin-up channel, (c) their simulated PL line-shapes, and (d) the geometry of the SiV center (split-vacancy) with D3d symmetry. Supercell visualization made with OVITO Basic (version 3.10.3) [35].

screening, achieving reliable results with reduced computational overhead.

2.2 | Luminescent Thermometry

As described previously, the sample synthesized at 40 Torr and 1.0% CH_4 was selected for analyzing its application in luminescent thermometry. To gain a more comprehensive understanding of the selected 40 Torr, 1.0% CH_4 diamond film, scanning electron microscopy (SEM), and cathodoluminescence (CL) analyses were performed. The SEM images confirmed a homogeneous film composed of well-faceted diamond crystals, while CL spectra, recorded at 83 K, revealed the characteristic SiV^- ZPL and its PSB, consistent with the PL measurements. These results, provided in detail in the (Figure S6), reinforce the high crystallinity of the sample and the robustness of the SiV^- emission under different excitation conditions, supporting its potential as a reliable optically active center.

Overall, the comprehensive physicochemical characterization indicates that the 40 Torr, 1.0% CH_4 Si-doped diamond sample was successfully grown by MWPECVD, exhibiting good crystallinity and promising SiV^- emission features. This sample will be further investigated in the following section through temperature-dependent PL to assess its potential for luminescent thermometry.

2.2.1 | Single Parametric Approach

Si-doped diamonds are now tested as luminescent thermometers. PL spectra of the selected sample were acquired using a 633 nm laser as the excitation source and recorded at different temperatures within the physiological range, between 300 and 325 K. To ensure reproducibility and statistical reliability, three independent measurements were performed at each temperature, and each measurement consisted of a scan of 100 individual spectra. Each spectrum shown in Figure 4a results from the average of these hundred scans at the relevant target temperature, providing a robust representation of the emission. As previously described in the characterization section, all PL spectra were post-processed by subtracting the baseline to isolate the emission signal corresponding to the SiV^- center and its associated PSB. This careful procedure allowed for a precise analysis of the temperature-dependent behavior of the SiV^- emission, as shown in Figure 4a, where both the ZPL and the PSB are clearly identified.

With increasing temperature, a noticeable decrease in the PL intensity of the SiV^- ZPL is observed, reflecting the expected thermal quenching of the optical center, despite the very short temperature range analyzed. To quantitatively extract the relevant thermometric parameters, namely, the peak intensity, FWHM, and integrated area of the ZPL, a Gaussian fitting procedure was applied to the SiV^- ZPL at each temperature, as shown in Figure 4b. This fitting provided precise values for each parameter, enabling a systematic analysis of the emission behavior as a function of temperature. Detailed fitting procedures, fitting curves, and statistical parameters are provided in Figure S7 in the (section S4).

Figure 5a shows these values for SiV^- emission centers as a function of temperature. In general, the intensity and integrated area of the photoluminescence peak are expected to decrease with increasing temperature, as thermal energy promotes electrons into non-radiative relaxation pathways. Irrespective of the specific mechanism involved, the FWHM is anticipated to broaden

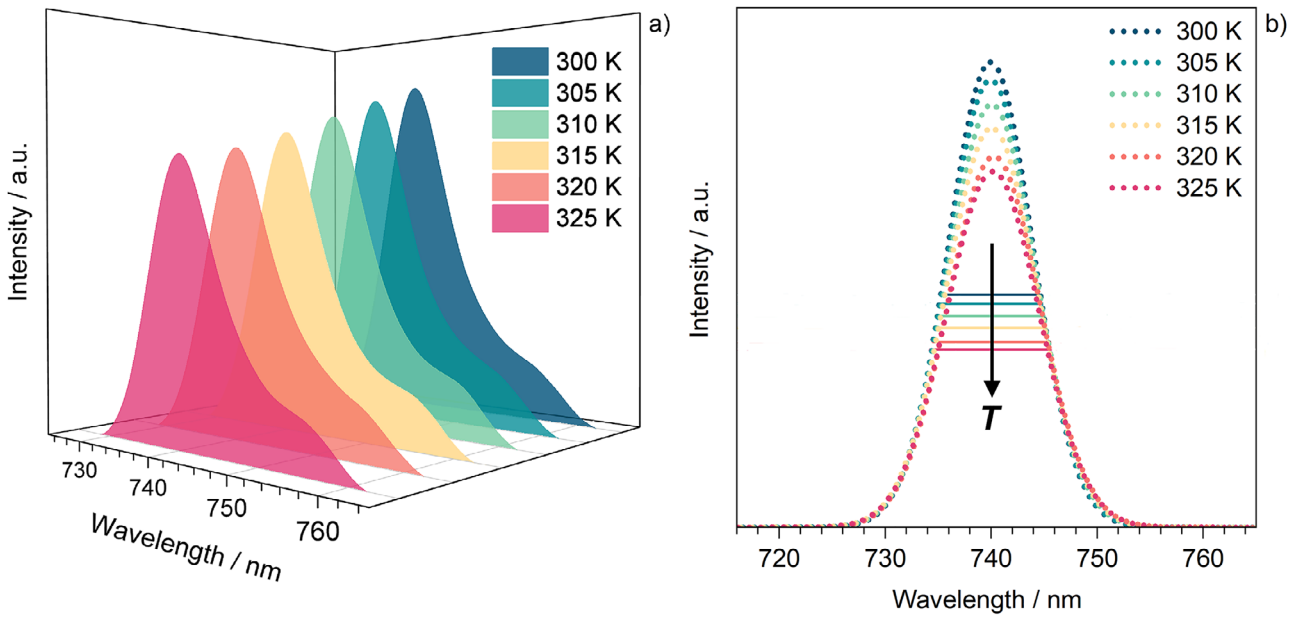

FIGURE 4 | (a) Temperature-resolved PL spectra, each spectrum resulting from the average of 100 spectra acquired in one spatial scan at a target temperature. (b) Gaussian fitting of the ZPL emission of SiV^- centers, from which luminescence descriptors are extracted.

with temperature due to the progressive population of higher vibrational states, which also contributes to the reduction of both the intensity and the area of the ZPL emission [18]. As shown in Figure 5a, the FWHM of the SiV^- ZPL peak increases as the temperature rises, while the corresponding intensity and area exhibit a marked decrease, consistent with the expected thermal behavior. To evaluate the suitability of each luminescence descriptor (Δ) for thermometric applications, the relative thermal sensitivity (S_r) was calculated according to

$$S_r\left(\%\ K^{-1}\right) = \frac{1}{\Delta T}\left|\frac{\partial \Delta}{\partial T}\right| \cdot 100\% \quad (1)$$

Figure 5b displays the relative thermal sensitivities obtained for each parameter. Linear fitting of the experimental data provides the thermal calibration models that enable temperature determination from PL measurements. The extracted relative sensitivities range from 0.64 to 0.76%·K^{-1} for the area, 0.94–1.23%·K^{-1} for the intensity, and 0.35–0.39%·K^{-1} for the FWHM. Since a Gaussian function was used to fit the experimental data, the area of each Gaussian could be calculated from the amplitude and the FWHM, so the sensitivity of the area is expected to be between the sensitivity of the intensity and the FWHM. Also, these results demonstrate that the intensity of the SiV^- ZPL emission exhibits the highest relative sensitivity among the evaluated descriptors, highlighting its relevance as the most reliable parameter for luminescent thermometry for these samples.

2.2.2 | Multiparametric Approach

Given the linear temperature dependence exhibited by the intensity, FWHM and integrated area of the SiV^- ZPL (see Figure 5a), it is attractive to implement a strategy that simultaneously exploits these descriptors to maximize S_r and enhance the overall thermometric performance of the material. One of the most effective approaches for this purpose is multiparametric linear regression (MLR), a statistical method that combines several independent variables to predict a dependent variable with higher accuracy.

In the context of luminescent thermometry, MLR allows the estimation of temperature (T) as a weighted linear combination of multiple thermometric parameters (Δ_i). For an effective application of MLR, the experimental data should satisfy the following statistical requirements: linear relationships between dependent and independent variables, low correlation among the independent variables, constant variance of residuals, independence of observations, and multivariate normality of the variables involved. Additionally, although not strictly necessary, feature scaling of the independent variables is recommended to ensure that all descriptors have comparable magnitudes, facilitating the interpretation of the regression coefficients [45].

Even though all three analyzed parameters exhibited linear behavior with temperature, to optimize the MLR model while minimizing interdependence between variables, the analysis was performed using the intensity and FWHM of the SiV^- ZPL emission only, because these two showed distinct temperature dependencies and complementary sensitivities. Therefore, our MLR model is able to obtain T values according to

$$T = \beta_0 + \sum_{i=1}^{2} \beta_i \Delta_i + \varepsilon \quad (2)$$

where β_0 is the intercept, Δ_i are the two thermometric parameters chosen, the intensity and FWHM of the SiV^- ZPL emission, β_i are the weighting coefficients associated with these two parameters, and ε is the residual error.

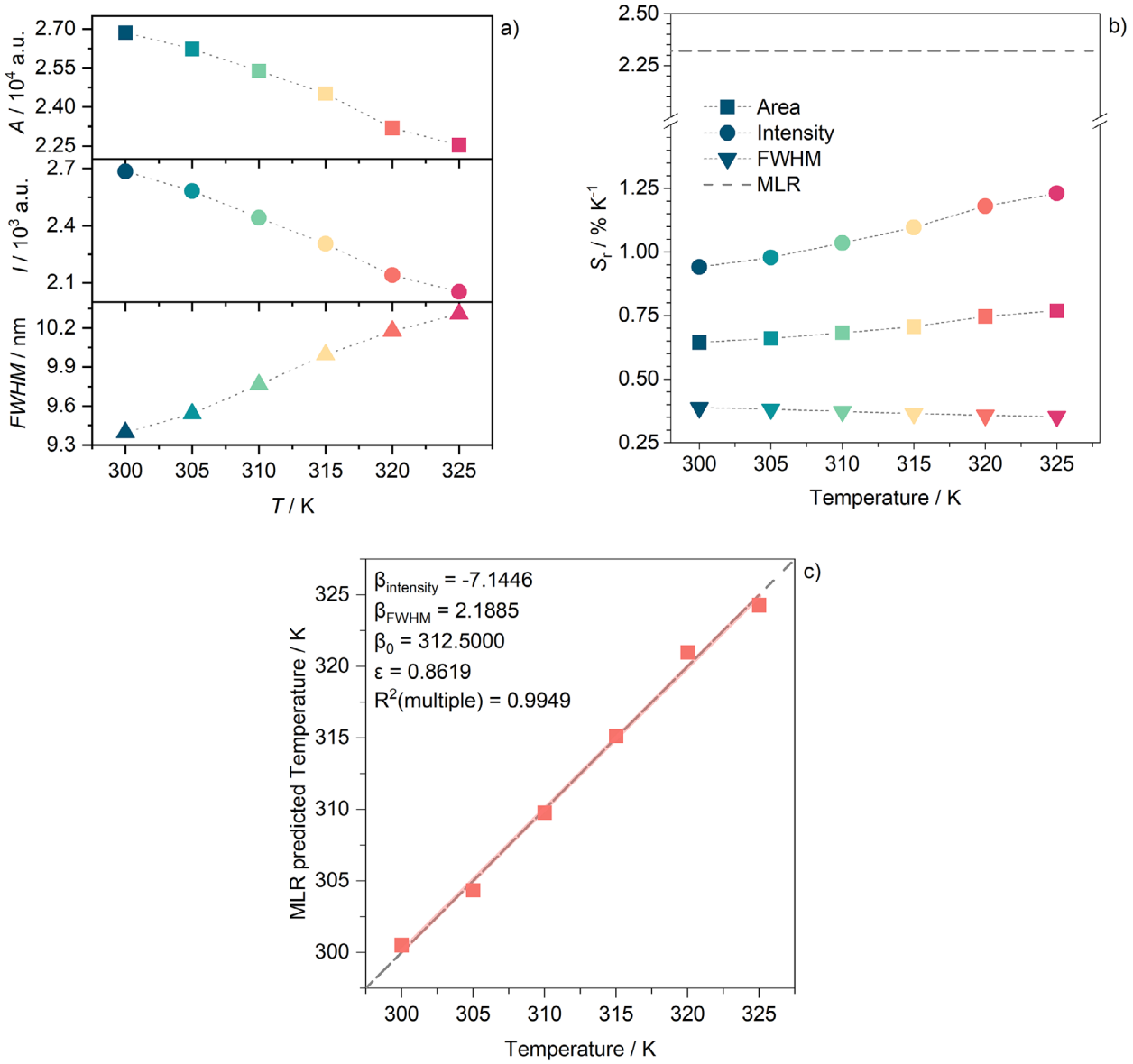

FIGURE 5 | (a) Evolution of the luminescence descriptors, area, intensity, and FWHM, extracted from ZPL peak of the SiV^- center, (b) relative thermal sensitivity obtained for the thermometric descriptors, area, intensity and FWHM and (c) MLR model prediction.

Figure 5c presents the comparison between the temperatures predicted by the MLR model and the experimental values. The weighting coefficients of the regression model are also included in the Figure 5c. As observed, only minor deviations are found throughout the entire temperature range analyzed, indicating the high accuracy of the regression model designed.

Maturi et al. [13] reported the general expression of the relative thermal sensitivity for MLR thermometry, which can be adapted for our MLR model as:

$$S_r^{MLR} = \sqrt{\sum_{i=1}^{2}\left(\frac{1}{\Delta_i}\left|\frac{\partial\Delta_i}{\partial T}\right|\right)^2} = \sqrt{\sum_{i=1}^{2}\left(\Delta_i\left|\frac{\partial T}{\partial\Delta_i}\right|\right)^{-2}} = \sqrt{\sum_{i=1}^{2}(\Delta_i\beta_i)^{-2}} \quad (3)$$

where, again, the two thermometric parameters in the sum are the intensity and FWHM of the SiV^- ZPL emission. The implementation of the MLR strategy significantly enhanced the thermometric response of the Si-doped diamond samples. By combining the intensity, which previously exhibited the highest individual sensitivity, with the FWHM, the maximum relative sensitivity reached a value of 2.3%·K^{-1}, nearly twice the sensitivity obtained using the intensity alone (see Figure 5b). This substantial improvement demonstrates the effectiveness of the multiparametric approach in increasing temperature resolution and overall sensing performance, confirming its suitability for precise luminescent thermometry within the physiological temperature range using the diamonds with SiV^- centers designed in this work.

While the MLR analysis demonstrates a highly sensitive and robust thermal response within the 300–325 K window, these measurements evaluate the fundamental physical response of the material. True biological environments possess complex ionic strengths, dynamic pH levels, and protein coronas that could induce surface band-bending and influence the SiV charge-state

stability. Although the chemically inert diamond lattice provides intrinsic shielding for deeper color centers, empirical validation of this MLR thermometry model in biologically relevant media (e.g., physiological buffers and cellular microenvironments) remains a critical next step before drawing definitive conclusions regarding its in vivo applicability. In addition, it is now important to distinguish the NCD thin-film platform from free-floating fluorescent nanodiamond (FND) particle thermometry. The optical measurements presented herein represent an ensemble response from multiple SiV-containing nanograins within the excitation volume, rather than isolated single-particle emission. While single FNDs offer ultimate spatial resolution, they suffer from dynamic instability and migration in fluidic biological environments. In contrast, the NCD thin-film architecture is specifically advantageous for integration into solid-state biomedical devices. Conformally coating structural probes, such as optical fiber tips or implantable micro-needles, enables highly stable, localized thermal sensing where the spatial resolution is dictated by the probe geometry, completely circumventing the tracking challenges associated with dispersed nanoparticles.

3 | Conclusion

Si-doped nanocrystalline diamond films were successfully synthesized by MWPECVD under varying methane concentrations and pressure conditions, aiming to maximize PL intensity. The diamond phase was confirmed by XRD, Raman spectroscopy, and XPS. PL and CL analyses verified the existence of SiV^- color centers responsible for the optical emission. The emission of SiV^- centers is maximized at lower deposition pressures, in the range tested, where the sp^3 content is slightly lower, but maintaining the quality of the diamond structure, and Si doping is achieved. Also, intermediate CH_4 concentration represents an optimal compromise: it exhibits well-defined diamond diffraction peaks, moderate surface disorder, a high sp^3 fraction, and intense SiV^- emission.

The sample exhibiting the highest PL intensity was selected for an in-depth study of its luminescent thermometric behavior. Several thermometric descriptors, including the integrated area, intensity, and FWHM of the ZPL, were evaluated. The multiparametric analysis demonstrated that Si-doped nanocrystalline diamonds can effectively operate as luminescent thermometers. Notably, a high thermal sensitivity of up to $2.3\%\cdot K^{-1}$ was achieved using both the intensity and the FWHM of the SiV^- ZPL, highlighting the strong potential of these nanodiamonds for temperature sensing applications in the physiological temperature range in biological environments.

These experimental findings are further supported by first-principles DFT calculations, which modelled the electronic structure, optical transitions, and phonon-assisted PL spectra of SiV^- and SiV° centers. The theoretical results provide a rigorous microscopic understanding of the observed emission, confirm the dominance of the SiV^- charge state, and rationalize the exceptional optical stability and reproducibility of the PL signals, establishing a solid link between the center properties and luminescent performance.

Therefore, the present work should be regarded as a proof of concept demonstrating the feasibility of temperature sensing based on the temperature-dependent luminescence intensity of SiV^- centers in CVD-grown diamond. But the performance under application-specific conditions (e.g., biological media, surface functionalization, or nanostructured geometries) should be experimentally assessed in future studies.

4 | Methods

4.1 | Si-Doped Diamond Growth

Silicon wafers (<100> orientation) supplied by Ted Pella Inc. were diced into 5×5 mm^2 substrates. Two types of Si substrates were prepared: (a) nanodiamond seeded [46] substrates for nanocrystalline diamond (NCD) growth and (b) non-seeded Si pieces used as sacrificial silicon sources for Si doping, placed near the seeded samples during CVD. The diamond growth process consisted of three main steps: (i) cleaning, (ii) nanodiamond seeding of the Si substrates, and (iii) growth of NCD films. A detailed description of each step is provided below.

Prior to deposition, all substrates underwent a degreasing process followed by plasma cleaning [46]. Degreasing was carried out by sequential immersion of the substrates in acetone and isopropanol, each for 15 min in an ultrasonic bath (Elma Transonic Tl-H-5, 80 kHz, 150 W). After cleaning, the substrates were dried under a nitrogen gas flow. To remove residual hydrocarbon contaminants and promote surface oxidation, an additional cleaning step using an oxygen plasma discharge was performed. The O_2 plasma treatment was carried out for 3 min in a home-built vacuum system, with an O_2 flow rate of 50 sccm, working pressure of 5 mTorr, and power of 200 W.

The seeding step is crucial to achieve uniform NCD films, as it significantly reduces the incubation time required for diamond nucleation [47]. The silicon substrates were seeded using a nanodiamond colloidal suspension, prepared by diluting a detonation nanodiamond slurry in deionized water to a concentration of 0.33 g l^{-1}. The colloid was deposited by spin coating, following the next procedure: (i) 500 rpm for 5 s, (ii) rinsed with deionized water for 15 s at 4000 rpm, and (iii) dried at 4000 rpm for 25 s. This method provides a high seeding density (*ca.* 10^{11} seeds·cm^{-2}), essential for obtaining smooth nanocrystalline diamond films.

The Si-doped nanodiamond films were synthesized in an ASTeX 6500 series MWPECVD system. The seeded Si substrates were positioned at the center of the substrate holder, while the non-seeded Si pieces were placed around them to act as sacrificial sources of silicon for in situ doping. The temperature was monitored using a Williamson Pro92 dual-wavelength pyrometer. Finally, film thickness was monitored in situ during deposition using a 405 nm laser interferometer. The specific growth conditions for each sample are summarized in Table 1. Also, the power for all growths was set at 2.5 kW. The growth quality was analyzed according to two parameters, the pressure and the percentage of methane. The pressure was varied from 40 to 80 Torr. Next, three different percentages of methane in the CVD plasma, i.e. 0.5%, 1.0%, and 1.5%, were tested at 40 Torr. This pressure was selected because it produces the best results according to the

photoluminescence emission, as discussed below. In addition, Figure S8 shows optical photographs of the grown diamonds, while Table 1 includes their size.

4.2 | Characterization of Si-Doped Diamonds

The synthesized diamond films were characterized to confirm the formation of the diamond structure under the different growth conditions. X-Ray diffraction (XRD) patterns were collected using a Bruker D8 Advance A-25 diffractometer equipped with a Lynxeye detector and a Cu-Kα radiation source. Measurements were performed over a 2θ range of 40°–80° with a step size of 0.030°, at 40 kV, and 40 mA, allowing the identification of the crystalline phase and assessment of the structural quality of the films. Raman spectroscopy was employed to detect the presence of different carbon allotropes. Spectra were recorded using a Horiba LabRAM HR Evolution modular spectrometer equipped with a Sincerity visible detector, using a 532 nm diode-pumped solid-state (DPSS) laser for excitation. In addition, X-ray photoelectron spectroscopy (XPS) was used for analyzing the chemical state bonding of the elements in the samples. XPS spectra were registered by using a Kratos Axis Ultra DLD spectrophotometer. This technique enabled detailed characterization of the different C atoms present in the samples, which led to an analysis of the quality of the diamonds grown. Steady-state photoluminescence (PL) spectra were acquired at room temperature to evaluate Si-doping and to study the emission features of the samples. PL measurements were performed using a He-Ne laser emitting at 633 nm (Pacific LasertecTM). Also, the sample exhibiting the most promising photoluminescence properties was further analyzed by cathodoluminescence (CL) spectroscopy. CL measurements were performed using a TESCAN Solaris dual-beam focused ion beam/field emission scanning electron microscope (FIB/FE-SEM) coupled to a Horiba iHR320 spectrometer. The luminescence was collected through a retractable parabolic mirror and analyzed with a monochromator equipped with a 600 grooves/mm grating and a Synapse CCD detector. Low-temperature measurements were conducted at 83 K using a liquid nitrogen-cooled stage (Quorum Technologies PP-3005), with SEM excitation set at 20 keV and 20 nA.

To evaluate the suitability of Si-doped diamonds for luminescent thermometry, temperature-dependent PL spectra were recorded using the Horiba LabRAM HR Evolution spectrometer coupled to a Cryotherm cryostat with a LakeShore 335 temperature controller, under vacuum. The system configuration is in backscattering mode by using a confocal microscope. The objective lens used is a long focal length lens with a magnification of 50x, and a numerical aperture of 0.50. A 633 nm laser was used for these measurements, enabling the study of the thermal response of the emission features. The estimated laser focus spot size is ∼2 μm. For the quantitative analysis of temperature-dependent PL data, including multi-parameter correlations and multiple linear regression, R Commander [48] was employed, providing a robust statistical treatment of the experimental results.

Furthermore, this characterization was completed with Fourier transform infrared (FTIR) spectroscopy measurements in diffuse reflectance mode, using a Bruker Tensor37 spectrophotometer, recording reflectance spectra in the range between 4000 and 400 cm^{-1}, with a resolution of 1 cm^{-1}. In turn, using the same equipment described above, luminescence spectra were obtained using a 473 nm laser as the excitation source, recording the emission spectra in the range between 500 and 800 nm.

4.3 | DFT Simulation of PL Line-Shapes

First-principles simulations of PL line-shapes for point defects pose a challenge due to the mathematical treatment of the electron-phonon coupling. The evaluation of the overlap integrals in the optical spectral function requires the solution of a many-body Schrödinger equation with $3N$ ionic degrees of freedom, in addition to the electronic degrees of freedom. The pioneering work of Alkauskas et al. [49] established a framework based on the generating function approach of Lax [50] and Kubo and Toyozawa [51], where they adopt the Franck-Condon principle and the displaced harmonic oscillator approximation. Subsequent work by Jin et al. [42] validated this approach in a theoretical and experimental study focusing on the negatively charged nitrogen-vacancy centers in diamond and the neutral divacancy centers in hexagonal SiC.

More recently, Tawfik and Russo [52] have translated this framework into PyPhotonics, an open-source Python code that streamlines PL line-shape simulations from density functional theory (DFT) calculations. PyPhotonics (version 0.2.0) workflow requires three inputs from VASP (version 6.4.3) [53–56] and phonopy (version 2.20) [57, 58]: the ground-state equilibrium structure and vibrational modes, and the excited-state equilibrium structure.

Here, we operate with diamond supercells containing a single SiV defect, which is created by removing two carbon atoms and placing a silicon atom in a split-vacancy configuration. Electronic structure calculations were performed using $3 \times 3 \times 3$ supercells (and a $3 \times 3 \times 3$ Γ-centred k-point mesh), whereas vibrational modes were computed using smaller $2 \times 2 \times 2$ supercells (and a $5 \times 5 \times 5$ Γ-centred k-point mesh). This choice represents a compromise between computational efficiency and accuracy for each relevant purpose. All VASP calculations were performed using the Perdew-Burke-Ernzerhof (PBE) functional [59] to describe the exchange-correlation term in the Kohn-Sham equations. Valence wave functions were described by sets of plane waves with kinetic energies up to 520 eV. Interactions between valence electrons and ionic cores were described using the projector-augmented wave (PAW) pseudopotentials [60, 61], where electron states up to 1s in C and 2p in Si are frozen to atomic reference states. Spin polarization was considered. The negatively charged center (SiV^-) includes an extra electron in the supercell, compensated by a positive background charge. Monopole corrections were added to address long-range electrostatics between the point defect in the charged supercell and its periodic images due to finite size.

Supercells were first optimized to their ground-state equilibrium structure using the conjugate gradient algorithm, with electronic and ionic convergence criteria set to 10^{-6} eV and 10^{-5} eV $Å^{-1}$, respectively. After relaxation, the ground-state electronic structure was characterized through calculations of the total density of states (DOS), the projected DOS (PDOS), and

the band structure. For DOS calculations, a denser 6 × 6 × 6 Γ-centered k-point mesh was used. Band structure was computed along the Γ–X–W–K–L–U–W–L–K|U–X k-path, generated with VASPKIT (version 1.5.1) [62], with 10 points per line.

Vibrational modes were obtained using the finite-displacements method implemented in phonopy [57, 58]. Force constants are obtained from forces on atoms in a series of structures generated by symmetry-consistent atomic displacements. A single-point VASP calculation was performed for each structure.

Excited state configurations were investigated using constrained configurations DFT (cDFT, also named delta-consistent field, ΔSCF). The occupation of spin-up and spin-down components was specified and kept fixed during the ionic relaxation. We set occupied states with integral occupation only. State energies were updated but the order was preserved to prevent inconsistent occupations [40, 63]. The relevant excited state results from promoting an electron from one of e_u states of the point-defect below the valence band edge to one of its e_g states within the gap.

Acknowledgements

M.G.G. and I.C.-B. thank Sherif A. Tawfik for insightful discussions on the use of PyPhotonics.

Funding

This research is part of the R&D&I project PID2023-150345OB-I00, funded by MICIU/AEI/10.13039/501100011033 and ERDF/EU. This work was also supported by Ministerio de Ciencia, Innovación y Universidades del Gobierno de España, which funds M.G.'s predoctoral position at the University of Cádiz in the form of an FPU fellowship (Grant No. FPU23/01837). KH and PP acknowledge funding from UHasselt Special Research Fund (BOF) via Methusalem NANO network, iBOF project IBOF-23-065, and BOF project BOF21GP05.

Conflicts of Interest

The authors declare no conflicts of interest.

Data Availability Statement

Data will be made available on request.

References

1. Y. Shen, J. Lifante, I. Zabala-Gutierrez, et al., "Reliable and Remote Monitoring of Absolute Temperature During Liver Inflammation via Luminescence-Lifetime-Based Nanothermometry," *Advanced Materials* 34 (2022): 2107764, https://doi.org/10.1002/adma.202107764.

2. H. Zhu, Y. Li, R. Qiu, L. Shi, W. Wu, and S. Zhou, "Responsive Fluorescent Bi_2O_3@PVA Hybrid Nanogels for Temperature-Sensing, Dual-Modal Imaging, and Drug Delivery," *Biomaterials* 33 (2012): 3058–3069, https://doi.org/10.1016/j.biomaterials.2012.01.003.

3. A. Bednarkiewicz, L. Marciniak, and L. D. Carlos, "Standardizing Luminescence Nanothermometry for Biomedical Applications," *Nanoscale* 12 (2020): 14405–14421, https://doi.org/10.1039/D0NR03568H.

4. C. D. S. Brites, R. Marin, M. Suta, et al., "Spotlight on Luminescence Thermometry: Basics, Challenges, and Cutting-Edge Applications," *Advanced Materials* 35 (2023): 2302749, https://doi.org/10.1002/adma.202302749.

5. B. del Rosal, E. Ximendes, U. Rocha, and D. Jaque, "In Vivo Luminescence Nanothermometry: From Materials to Applications," *Advanced Optical Materials* 5 (2017): 1600508, https://doi.org/10.1002/adom.201600508.

6. Y. Takei, S. Arai, A. Murata, et al., "A Nanoparticle-Based Ratiometric and Self-Calibrated Fluorescent Thermometer for Single Living Cells," *ACS Nano* 8 (2014): 198–206, https://doi.org/10.1021/nn405456e.

7. D. Jaque, B. del Rosal, E. M. Rodríguez, L. M. Maestro, P. Haro-González, and J. G. Solé, "Fluorescent Nanothermometers for Intracellular Thermal Sensing," *Nanomedicine* 9 (2014): 1047–1062, https://doi.org/10.2217/nnm.14.59.

8. A. Cadiau, C. D. S. Brites, P. M. F. J. Costa, R. A. S. Ferreira, J. Rocha, and L. D. Carlos, "Ratiometric Nanothermometer Based on an Emissive Ln^{3+}-Organic Framework," *ACS Nano* 7 (2013): 7213–7218, https://doi.org/10.1021/nn402608w.

9. A. Benayas, B. del Rosal, A. Pérez-Delgado, K. Santacruz-Gómez, D. Jaque, and G. A. Hirata, "Nd:YAG Near-Infrared Luminescent Nanothermometers," *Advanced Optical Materials* 3 (2015): 687–694, https://doi.org/10.1002/adom.201400484.

10. W. Piotrowski, M. Kuchowicz, M. Dramićanin, and L. Marciniak, "Lanthanide Dopant Stabilized Ti^{3+} State and Supersensitive Ti^{3+} - Based Multiparametric Luminescent Thermometer in $SrTiO_3$:Ln^{3+} (Ln^{3+} = Lu^{3+}, La^{3+}, Tb^{3+}) Nanocrystals," *Chemical Engineering Journal* 428 (2022): 131165, https://doi.org/10.1016/j.cej.2021.131165.

11. S. Sotoma, C. P. Epperla, and H. Chang, "Diamond Nanothermometry," *ChemNanoMat* 4 (2018): 15–27, https://doi.org/10.1002/cnma.201700257.

12. S. Choi, V. N. Agafonov, V. A. Davydov, L. F. Kulikova, and T. Plakhotnik, "Formation of Interstitial Silicon Defects in Si- and Si,P-Doped Nanodiamonds and Thermal Susceptibilities of SiV − Photoluminescence Band," *Nanotechnology* 31 (2020): 205709, https://doi.org/10.1088/1361-6528/ab72bb.

13. F. E. Maturi, C. D. S. Brites, E. C. Ximendes, et al., "Going Above and Beyond: A Tenfold Gain in the Performance of Luminescence Thermometers Joining Multiparametric Sensing and Multiple Regression," *Laser & Photonics Reviews* 15 (2021): 2100301, https://doi.org/10.1002/lpor.202100301.

14. T. A. Alrebdi, A. N. Alodhayb, Z. Ristić, and M. D. Dramićanin, "Comparison of Performance Between Single- and Multiparameter Luminescence Thermometry Methods Based on the Mn^{5+} Near-Infrared Emission," *Sensors* 23 (2023): 3839, https://doi.org/10.3390/s23083839.

15. M. Bin Afif, A. Mesbahi, A. Altakhov, and D. Choi, "Growth and Characterization of Large Single Crystal Diamond Grown by MPCVD With Varying Methane Concentration," *Materials Today Communications* 51 (2026): 114715, https://doi.org/10.1016/j.mtcomm.2026.114715.

16. J. Lu, B. Yang, B. Yu, et al., "Fabrication of Diamond Nanoneedle Arrays Containing High-Brightness Silicon-Vacancy Centers," *Advanced Optical Materials* 9 (2021): 2101427, https://doi.org/10.1002/adom.202101427.

17. Y. Chen, T. Tao, H. Yu, et al., "SiV Color Center Concentration Enhancement by Rapid Thermal Annealing of Si-Doped MPCVD Diamonds," *Applied Physics A* 131 (2025): 366, https://doi.org/10.1007/s00339-025-08488-w.

18. M. Rodríguez-Fernández, M. Gragera, I. Carrillo-Berdugo, et al., "N-/Si-Co-Doped Nanocrystalline Diamonds as Highly Sensitive Luminescent Thermometers," *Nanoscale* 17 (2025): 14134–14144, https://doi.org/10.1039/D4NR04132A.

19. Y. Cui, J. Zhang, F. Sun, and Z. Zhang, "Si-Doped Diamond Films Prepared by Chemical Vapour Deposition," *Transactions of Nonferrous Metals Society of China* 23 (2013): 2962–2970, https://doi.org/10.1016/S1003-6326(13)62821-6.

20. B. Yang, J. Li, L. Guo, et al., "Fabrication of Silicon-Vacancy Color Centers in Diamond Films: Tetramethylsilane as a New Dopant Source," *CrystEngComm* 20 (2018): 1158–1167, https://doi.org/10.1039/C7CE02181J.

21. R. Richter, M. I. S. Röhr, T. Zimmermann, et al., "Laser-Induced Fluorescence of Free Diamondoid Molecules," *Physical Chemistry Chemical Physics* 17 (2015): 4739–4749, https://doi.org/10.1039/C4CP04423A.

22. T. Yeghoyan, K. Alassaad, V. Soulière, G. Ferro, M. Gutierrez, and D. Araujo, "How to Grow Fully (100) Oriented SiC/Si/SiC/Si Multi-Stack," *Physica Status Solidi* 216 (2019): 201800588, https://doi.org/10.1002/pssa.201800588.

23. S. Drijkoningen, S. D. Janssens, P. Pobedinskas, S. Koizumi, M. K. Van Bael, and K. Haenen, "The Pressure Sensitivity of Wrinkled B-Doped Nanocrystalline Diamond Membranes," *Scientific Reports* 6 (2016): 35667, https://doi.org/10.1038/srep35667.

24. S. Reich and C. Thomsen, "Raman Spectroscopy of Graphite," *Philosophical Transactions of the Royal Society of London Series A: Mathematical, Physical and Engineering Sciences* 362 (2004): 2271–2288, https://doi.org/10.1098/rsta.2004.1454.

25. V. Zólyomi, J. Koltai, and J. Kürti, "Resonance Raman Spectroscopy of Graphite and Graphene," *Basic Solid State Physics* 248 (2011): 2435–2444, https://doi.org/10.1002/pssb.201100295.

26. J. Millán-Barba, A. Taylor, H. Bakkali, et al., "Low Temperature Growth of Nanocrystalline Diamond: Insight Thermal Property," *Diamond and Related Materials* 137 (2023): 110070, https://doi.org/10.1016/j.diamond.2023.110070.

27. T. Kageura, K. Takemura, M. Maeda, A. Otake, Y. Einaga, and S. Ohmagari, "Tuning sp^3/sp^2 Carbon Ratio of Heavily Boron-Doped Diamond Electrodes Fabricated via Hot-Filament Chemical Vapour Deposition With CO_2 Addition," *Scientific Reports* 15 (2025): 41095, https://doi.org/10.1038/s41598-025-25010-7.

28. L. Yang, C. Jiang, S. Guo, et al., "Novel Diamond Films Synthesis Strategy: Methanol and Argon Atmosphere by Microwave Plasma CVD Method Without Hydrogen," *Nanoscale Research Letters* 11 (2016): 415, https://doi.org/10.1186/s11671-016-1628-x.

29. J. E. Butler, Y. A. Mankelevich, A. Cheesman, J. Ma, and M. N. R. Ashfold, "Understanding the Chemical Vapor Deposition of Diamond: Recent Progress," *Journal of Physics: Condensed Matter* 21 (2009): 364201, https://doi.org/10.1088/0953-8984/21/36/364201.

30. D. G. Goodwin, "Scaling Laws for Diamond Chemical-Vapor Deposition. I. Diamond Surface Chemistry," *Journal of Applied Physics* 74 (1993): 6888–6894, https://doi.org/10.1063/1.355063.

31. P. W. May, "Diamond Thin Films: A 21st-Century Material," *Philosophical Transactions of the Royal Society of London Series A: Mathematical, Physical and Engineering Sciences* 358 (2000): 473–495, https://doi.org/10.1098/rsta.2000.0542.

32. J.-I. Kim, Y.-J. Jang, J. Kim, and J. Kim, "Effects of Silicon Doping on Low-Friction and High-Hardness Diamond-Like Carbon Coating via Filtered Cathodic Vacuum Arc Deposition," *Scientific Reports* 11 (2021): 3529, https://doi.org/10.1038/s41598-021-83158-4.

33. Y. Luo, X. Yang, L. Yue, D. S. Ren, and J. R. Chen, "Effect of Phosphorus Doping on the Luminescence Intensity of Si-NC in SiO/Si Multilayers," *Optics Express* 31 (2023): 24566, https://doi.org/10.1364/OE.494438.

34. J. Riedrich-Möller, C. Arend, C. Pauly, et al., "Deterministic Coupling of a Single Silicon-Vacancy Color Center to a Photonic Crystal Cavity in Diamond," *Nano Letters* 14 (2014): 5281–5287, https://doi.org/10.1021/nl502327b.

35. A. Stukowski, "Visualization and Analysis of Atomistic Simulation Data With OVITO–the Open Visualization Tool," *Modelling and Simulation in Materials Science and Engineering* 18 (2010): 015012, https://doi.org/10.1088/0965-0393/18/1/015012.

36. A. Gali and J. R. Maze, "Ab Initio Study of the Split Silicon-Vacancy Defect in Diamond: Electronic Structure and Related Properties," *Physical Review B* 88 (2013): 235205, https://doi.org/10.1103/PhysRevB.88.235205.

37. B. L. Green, M. W. Doherty, E. Nako, et al., "Electronic Structure of the Neutral Silicon-Vacancy Center in Diamond," *Physical Review B* 99 (2019): 161112, https://doi.org/10.1103/PhysRevB.99.161112.

38. M. Abdi, J.-P. Chou, A. Gali, and M. B. Plenio, "Color Centers in Hexagonal Boron Nitride Monolayers: A Group Theory and Ab Initio Analysis," *ACS Photonics* 5 (2018): 1967–1976, https://doi.org/10.1021/acsphotonics.7b01442.

39. G. Thiering and A. Gali, "The (eg ⊗ eu) ⊗ Eg product Jahn–Teller Effect in the Neutral Group-IV Vacancy Quantum Bits in Diamond," *Npj Computational Materials* 5 (2019): 18, https://doi.org/10.1038/s41524-019-0158-3.

40. Y. Xiong and G. Hautier, "ΔSCF in VASP for Excited-State Defect Computations: Tips and Pitfalls," preprint, bioRxiv, May 7, 2025, https://doi.org/10.48550/arXiv.2505.04748.

41. I. B. Bersuker, "The Jahn-Teller Effects in Chemical Reactions and Materials Science," *Journal of Physics: Conference Series* 2769 (2024): 012001, https://doi.org/10.1088/1742-6596/2769/1/012001.

42. Y. Jin, M. Govoni, and G. Galli, "Vibrationally Resolved Optical Excitations of the Nitrogen-Vacancy Center in Diamond," *Npj Computational Materials* 8 (2022): 238, https://doi.org/10.1038/s41524-022-00928-y.

43. Á. Gali, "Ab Initio Theory of the Nitrogen-Vacancy Center In Diamond," *Nanophotonics* 8 (2019): 1907–1943, https://doi.org/10.1515/nanoph-2019-0154.

44. S. Vimolchalao, W. H. Liang, F. D. Vila, J. J. Kas, F. Farges, and J. J. Rehr, "Bethe-Salpeter Equation Calculations of Nitrogen-Vacancy Defects in Diamond," *Journal of Physics and Chemistry of Solids* 122 (2018): 87–93, https://doi.org/10.1016/j.jpcs.2018.06.006.

45. E. V. Borisov, A. A. Kalinichev, and I. E. Kolesnikov, "Single- and Multiparametric Luminescence Cryogenic Thermometry Using ZnTe/CdTe Layers," *Optical Materials* 149 (2024): 114978, https://doi.org/10.1016/j.optmat.2024.114978.

46. P. Pobedinskas, G. Degutis, W. Dexters, J. D'Haen, M. K. Van Bael, and K. Haenen, "Nanodiamond Seeding on Plasma-Treated Tantalum Thin Films and the Role of Surface Contamination," *Applied Surface Science* 538 (2021): 148016, https://doi.org/10.1016/j.apsusc.2020.148016.

47. G. Degutis, P. Pobedinskas, H.-G. Boyen, et al., "Improved Nanodiamond Seeding on Chromium by Surface Plasma Pretreatment," *Chemical Physics Letters* 640 (2015): 50–54, https://doi.org/10.1016/j.cplett.2015.10.002.

48. A. J. Arriaza, F. Fernández, M. López, M. Muñoz, S. M. Pérez, and A. Sánchez, *Estadística Básica con R y R-Commander* (Universidad de Cádiz: Cadiz, 2008).

49. A. Alkauskas, B. B. Buckley, D. D. Awschalom, and C. G. Van de Walle, "First-Principles Theory of the Luminescence Lineshape for the Triplet Transition in Diamond NV Centres," *New Journal of Physics* 16 (2014): 073026, https://doi.org/10.1088/1367-2630/16/7/073026.

50. M. Lax, "The Franck-Condon Principle and Its Application to Crystals," *The Journal of Chemical Physics* 20 (1952): 1752–1760, https://doi.org/10.1063/1.1700283.

51. R. Kubo and Y. Toyozawa, "Application of the Method of Generating Function to Radiative and Non-Radiative Transitions of a Trapped Electron in a Crystal," *Progress of Theoretical Physics* 13 (1955): 160–182, https://doi.org/10.1143/PTP.13.160.

52. S. A. Tawfik and S. P. Russo, "PyPhotonics: A Python Package for the Evaluation of Luminescence Properties of Defects," *Computer Physics Communications* 273 (2022): 108222, https://doi.org/10.1016/j.cpc.2021.108222.

53. G. Kresse and J. Furthmüller, "Efficient Iterative Schemes for Ab Initio Total-Energy Calculations Using a Plane-Wave Basis Set," *Physical Review B* 54 (1996): 11169–11186, https://doi.org/10.1103/PhysRevB.54.11169.

54. G. Kresse and J. Hafner, "Ab Initio Molecular-Dynamics Simulation of the Liquid-Metal–Amorphous-Semiconductor Transition in Germanium," *Physical Review B* 49 (1994): 14251–14269, https://doi.org/10.1103/PhysRevB.49.14251.

55. G. Kresse and J. Furthmüller, "Efficiency of Ab-Initio Total Energy Calculations for Metals and Semiconductors Using a Plane-Wave Basis

Set," *Computational Materials Science* 6 (1996): 15–50, https://doi.org/10.1016/0927-0256(96)00008-0.

56. G. Kresse, D. Vogtenhuber, M. Marsman, M. Kaltak, F. Karsai, and M. Schlipf, Vienna Ab Initio Simulation Package (VASP) (2023), version 6.4.3.

57. A. Togo, "First-Principles Phonon Calculations With Phonopy and Phono3py," *Journal of the Physical Society of Japan* 92 (2023): 012001, https://doi.org/10.7566/JPSJ.92.012001.

58. A. Togo, L. Chaput, T. Tadano, and I. Tanaka, "Implementation Strategies in Phonopy and Phono3py," *Journal of Physics: Condensed Matter* 35 (2023): 353001, https://doi.org/10.1088/1361-648X/acd831.

59. J. P. Perdew, K. Burke, and M. Ernzerhof, "Generalized Gradient Approximation Made Simple," *Physical Review Letters* 77 (1996): 3865–3868, https://doi.org/10.1103/PhysRevLett.77.3865.

60. G. Kresse and J. Hafner, "Norm-Conserving and Ultrasoft Pseudopotentials for First-Row and Transition Elements," *Journal of Physics: Condensed Matter* 6 (1994): 8245–8257, https://doi.org/10.1088/0953-8984/6/40/015.

61. G. Kresse and D. Joubert, "From Ultrasoft Pseudopotentials to the Projector Augmented-Wave Method," *Physical Review B* 59 (1999): 1758–1775, https://doi.org/10.1103/PhysRevB.59.1758.

62. V. Wang, N. Xu, J.-C. Liu, G. Tang, and W.-T. Geng, "VASPKIT: A User-Friendly Interface Facilitating High-Throughput Computing and Analysis Using VASP Code," *Computer Physics Communications* 267 (2021): 108033, https://doi.org/10.1016/j.cpc.2021.108033.

63. O. Bulancea-Lindvall, J. Davidsson, I. G. Ivanov, et al., "Temperature dependence of the AB lines and optical properties of the carbon–antisite-vacancy pair in 4H−SiC," *Physical Review Applied* 22 (2024): 0343056, https://doi.org/10.1103/PhysRevApplied.22.034056.

Supporting Information

Additional supporting information can be found online in the Supporting Information section.

Supporting File: adfm77324-sup-0001-SuppMat.pdf.